Available online at www.sciencedirect.com
SCIENCE DIRECT®
Vacuum 73 (2004) 93–104
VACUUM
SURFACE ENGINEERING, SURFACE INSTRUMENTATION & VACUUM TECHNOLOGY
www.elsevier.com/locate/vacuum

Ion-beam-defect processes in group-III nitrides and ZnO

S.O. Kucheyev[a,*], J.S. Williams[b], C. Jagadish[b]

[a] *Lawrence Livermore National Laboratory, Livermore, CA 94550, USA*
[b] *Department of Electronic Materials Engineering, Research School of Physical Sciences and Engineering, The Australian National University, Canberra, ACT 0200, Australia*

Received 29 August 2003; accepted 1 December 2003

Abstract

Recently, there has been much interest in wide band-gap wurtzite semiconductors such as group-III nitrides (GaN, AlGaN, and InGaN) and ZnO. Ion-beam-defect processes are considerably more complex in these wurtzite semiconductors than in the case of both elemental and group-III–V cubic semiconductors. This brief review focuses on our recent studies of the following aspects of ion-beam-defect processes: (i) effects of implanted species and the density of collision cascades, (ii) the nature of ion-beam-produced planar defects in GaN, (iii) defect production in GaN by swift heavy ions, (iv) blistering of H-implanted GaN, (v) electrical isolation of GaN and ZnO, (vi) the effect of Al and In content on defect processes in III-nitrides, and (vii) structural damage in ZnO with an intriguing effect of the formation of an anomalous defect peak. Emphasis is given to unusual ion-beam-defect processes and to the physical mechanisms underlying them.

PACS: 61.72.Cc; 61.72.Dd; 68.55.Ln; 61.72.Vv

Keywords: Ion implantation; Amorphization; GaN; ZnO; Defects; Isolation; Blistering

1. Introduction

Important applications of wide band-gap wurtzite semiconductors such as group-III nitrides (GaN, AlGaN, and InGaN) and ZnO in (opto)electronics have stimulated extensive research efforts over the past decade (see, for example, reviews [1,2]). In the fabrication of ZnO- and III-nitride-based devices, ion bombardment represents a rather attractive processing tool for several technological steps, including selective-area doping, electrical and optical isolation, dry etching, and ion slicing. However, ion-beam-produced lattice disorder and its often undesirable consequences limit technological applications of ion implantation.

Ion-beam-defect processes in GaN have recently been reviewed in [3–5]. In particular, it has been shown that *dynamic annealing* processes (i.e., defect interaction processes) are extremely efficient in GaN even during heavy-ion bombardment at low temperatures [4]. The intriguing damage-related processes in GaN, discussed in detail in review [4], include (i) complex damage buildup behaviour with defect saturation in the crystal

*Corresponding author.
E-mail address: kucheyev1@llnl.gov (S.O. Kucheyev).

0042-207X/$ - see front matter © 2003 Elsevier Ltd. All rights reserved.
doi:10.1016/j.vacuum.2003.12.032

bulk, (ii) preferential surface disordering and nitrogen loss, (iii) ion-beam-induced porosity and associated material decomposition, (iv) anomalous surface erosion at elevated temperatures, and (v) the reconstruction of amorphous GaN by light-ion re-irradiation.

Since our last review [4], the field of ion implantation into III-nitrides has matured significantly. Indeed, for the past two years, a number of detailed studies of ion-beam-produced lattice defects in GaN, AlGaN, AlN, and InGaN (as well as in another wurtzite semiconductor, ZnO) have been reported. The present brief review mainly concentrates on our recent progress made in the understanding of ion-beam processes in III-nitrides and ZnO, not included in our previous review article [4]. Due to space limitations, we will discuss only the most unusual aspects of the ion-beam damaging behaviour in these materials.

2. Effects of ion species and collision cascade density on defect processes in GaN

A detailed study of the effect of ion species and the density of collision cascades on defect accumulation in GaN at liquid nitrogen (LN_2) and room temperatures (RT) has recently been reported in [6–8]. Fig. 1 shows the dose dependence of maximum relative disorder in the crystal bulk for several ion species at LN_2 [Fig. 1(a)] and RT [Fig. 1(b)], as measured by Rutherford backscattering/channelling spectrometry (RBS/C). It is seen from Fig. 1(a) that GaN exhibits bulk amorphization at LN_2 (with the formation of buried amorphous layers) only for very heavy ions (such as ^{197}Au and ^{209}Bi) and for light ^{12}C and ^{16}O ions. However, in the case of bombardment with intermediate-mass ions studied (^{28}Si, ^{63}Cu, and ^{107}Ag), Fig. 1 shows that the damage level in the bulk saturates, and amorphization proceeds only from the surface for both LN_2 and RT bombardment regimes. Hence, ion mass affects not only the level of implantation-produced lattice disorder but also the main features of the damage buildup behaviour in GaN.

To better illustrate the effects of ion species on the level of pre-amorphous disorder in GaN, Fig. 2

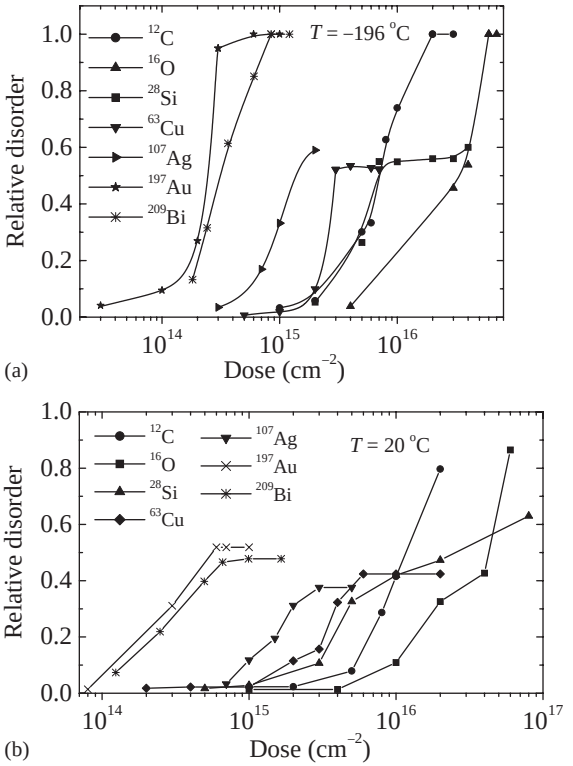

Fig. 1. Maximum relative disorder (extracted from RBS/C spectra) in the bulk defect peak as a function of dose for 40 keV C, 50 keV O, 60 keV Si, 130 keV Cu, 200 keV Ag, 300 keV Au, and 500 keV Bi ions implanted at LN_2 (a) and RT (b), as indicated in the legend.

(the left axis) shows the ion mass dependence of the ion doses required to produce 30% relative disorder, $\Phi_{0.3}$, at LN_2 [Fig. 2(a)] and RT [Fig. 2(b)]. Such ion doses, $\Phi_{0.3}$, have been found by interpolation of damage build-up curves from Fig. 1. It is seen from Fig. 2 (the left axis) that $\Phi_{0.3}$ generally decreases with increasing ion mass. This qualitative trend is expected since the number of ion-beam-generated atomic displacements increases with ion mass.

However, two deviations from the trend expected are clearly seen in Fig. 2 for the cases of ^{12}C and ^{209}Bi ions for both LN_2 and RT bombardment regimes. For example, $\Phi_{0.3}$ for ^{12}C ions is about two times smaller than $\Phi_{0.3}$ for ^{16}O ions for both LN_2 and RT, despite the fact that ^{16}O ions produce $\sim$1.6 times more vacancies than ^{12}C ions in the maximum of the nuclear energy loss profile.

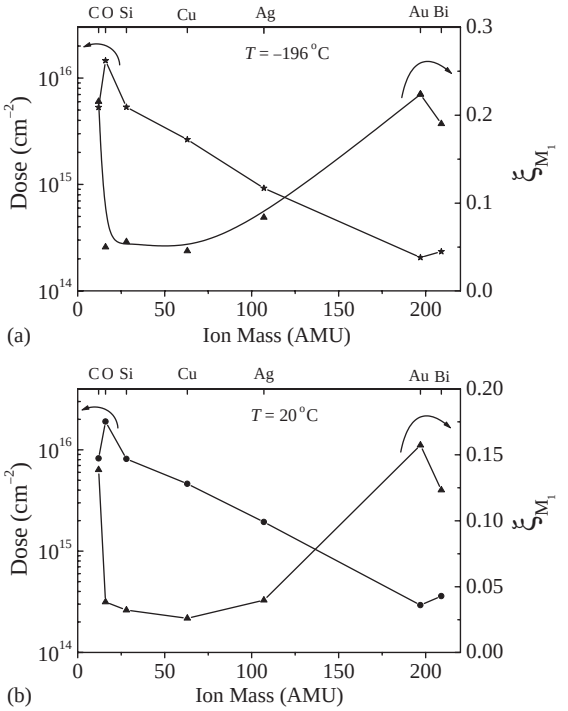

Fig. 2. Left axis: the ion mass dependence of the ion dose necessary to produce relative disorder of 0.3 (as measured by RBS/C) by implantation at LN_2 (a) and RT (b). Right axis: the dependence of ξ_{M_1} (ξ_{M_1} = the ratio of the level of lattice disorder measured experimentally to the damage level predicted based on ballistic calculations) on ion mass.

This is a somewhat extreme example of chemical effects of implanted species, consistent with the data for C shown in Fig. 1, as discussed in detail in [6]. In addition to ^{12}C, irradiation with ^{209}Bi ions produced less stable lattice damage than bombardment with ^{197}Au ions, although ^{209}Bi ions generate a larger number of atomic displacements than ^{197}Au ions. This result has been attributed to the lower beam flux value in the case of Bi ions compared with the beam flux value of Au ions [6].

A further insight into the effect of ion mass on implantation-produced lattice disorder in GaN is given in Fig. 2 (the right axis), which shows the ion mass dependence of ξ_{M_1}, the ratio of the level of lattice disorder of 0.3 (as measured by RBS/C) to the damage level predicted based on ballistic calculations $\Phi_{0.3}N_{vac}^{max}/n_{at}$, where N_{vac}^{max} is the number of lattice vacancies in the maximum of the nuclear energy loss profile, and n_{at} is the atomic concentration of GaN. In the first approximation, the parameter ξ_{M_1} reflects the effectiveness of the production of stable lattice disorder (N^{def}) by ion bombardment under particular implant conditions: $N^{def} = \xi_{M_1}\Phi N_{vac}^{max}$ for relatively low levels of lattice disorder, where Φ is ion dose. If postimplantation stable lattice damage were the same as the one predicted based on ballistic calculations (such as the TRIM code [9]), ξ_{M_1} would be equal to unity and independent of ion mass.

In contrast to such expectations, Fig. 2 (the right axis) shows a rather complex dependence of ξ_{M_1} on ion mass for both LN_2 and RT bombardment regimes. First of all, for all ion species used, ξ_{M_1} is significantly below unity. This is a direct consequence of strong dynamic annealing processes when a large fraction of ion-beam-generated point defects experiences annihilation even at LN_2. It is also seen from Fig. 2 (the right axis) that, with increasing ion mass from ^{12}C to ^{63}Cu, ξ_{M_1} decreases. For ions heavier than ^{63}Cu, ξ_{M_1} shows an increase with increasing ion mass. Such a complex behaviour has been attributed in [6] to a combination of the following factors: (i) strong dynamic annealing processes, (ii) changes in defect clustering efficiency, (iii) collective energy spike effects, (iv) variations in the effective displacement energy, and (v) chemical effects of implanted species.

3. Nature of planar defects in GaN

It has been established that irradiation under a wide range of implant conditions (such as ion mass, dose, and implant temperature) leads to the formation of planar defects which are parallel to the basal plane of the wurtzite structure of GaN [4,10]. An example of planar defects will be given in Section 7 [Fig. 6(b)]. The nature of such ion-irradiation-produced planar defects has recently been studied by high-resolution transmission electron microscopy (XTEM) in [11,12]. Interestingly, for all implant conditions studied in [12], all planar defects observed in the ~20-nm-thick near-surface layers of GaN are interstitial in nature and have Burgers vectors of either 1/2[0001] or

$1/6\langle 2\bar{2}03\rangle$. Although the nature of these irradiation-produced planar defects appears to be independent of implant conditions, irradiation parameters have been found to influence the average defect size and density. In particular, larger planar defects have been observed for higher irradiation temperatures.

It should be noted that irradiation-produced planar defects are a result of dynamic annealing processes occurring in GaN during ion bombardment even at liquid nitrogen temperature. Such planar defects are formed by migrating interstitials generated in different collision cascades. This is supported by the facts reported in [12] that (i) the average size of planar defects is, in many cases, larger than the lateral size of collision cascades (which are $\lesssim 10$ nm for the case of 300 keV Au ions, based on ballistic calculations such as the TRIM code [9]) and (ii) the size of planar defects increases with increasing ion dose.

It is also interesting to note that, although only interstitial-based defects have been identified in [12], the ion beam generates an equal number of lattice interstitials and vacancies. While interstitials agglomerate to form planar defects, vacancies can either migrate and annihilate at the sample surface or agglomerate into some stable vacancy-rich defect complexes. However, a long-range migration of vacancies to the sample surface seems to be unlikely, particularly for relatively high ion doses for which planar defects are experimentally observed. Indeed, in a crystal with a relatively large concentration of lattice defects, trap-limited short-range defect migration is expected to dominate long-range defect diffusion. The agglomeration of ion-beam-generated vacancies into some vacancy-rich defect complexes is, thus, more plausible [12].

4. Lattice damage produced in GaN by intense electronic excitation

In all the previous studies (see, for example, reviews [3,4]), it has been assumed that lattice defects are produced as a result of nuclear (or elastic) collisions, while electronic energy loss processes (i.e., the excitation of the electronic subsystem of the solid) have a negligible role in defect formation in GaN under bombardment with keV ions. Indeed, in the case of irradiation with keV ions, the level of electronic excitation is $\lesssim 1$ keV/nm. Such low electronic energy losses typically do not result in the formation of lattice defects in radiolysis-resistant materials such as GaN. The level of electronic excitation gradually increases with increasing ion energy and atomic number. Electronic energy losses can reach some tens of keV/nm in the case of heavy ions with energies of several hundred MeV. In this so-called swift heavy ion bombardment regime, intense ultrafast excitation of valence electrons occurs along ion tracks (see, for example, reviews [13,14]).

In order to understand the effect of intense electronic excitation on defect formation in GaN, lattice defects produced by 200 MeV $^{197}Au^{16+}$ ions have been studied in Ref. [15]. Fig. 3 shows bright-field XTEM images of GaN bombarded at 300 K with 200 MeV Au ions to a fluence of 2×10^{11} cm^{-2}. This figure illustrates the formation of near-continuous latent tracks, clearly visible even at low magnification. These tracks propagate throughout the entire GaN film into the sapphire substrate. No external defects such as dislocations or stacking faults are visible in the vicinity of the tracks. Analysis of selected-area diffraction

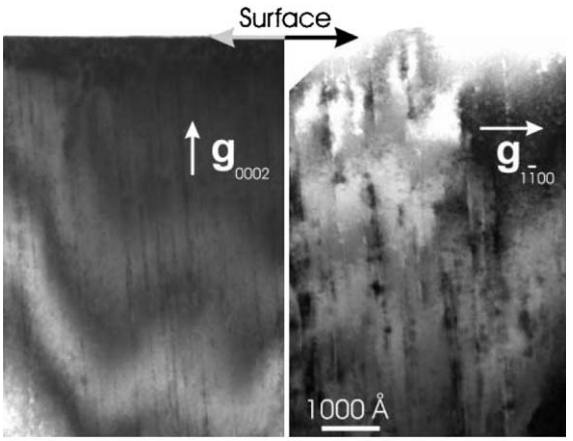

Fig. 3. Bright-field XTEM images [(a) $\mathbf{g} = 0002^*$ and (b) $\mathbf{g} = 1\bar{1}00^*$] of GaN bombarded at RT with 200 MeV Au ions with a beam flux of $\sim 3 \times 10^9$ cm^{-2} s^{-1} to a fluence of 2×10^{11} cm^{-2}. Both images are of the same magnification.

patterns from the sample shown in Fig. 3 has not revealed the presence of an amorphous phase [15]. Hence, the tracks appear to consist of a disordered material, resulting in lattice stress responsible for XTEM contrast. The fluence of 2×10^{11} cm^{-2} corresponds to an average distance between ion impacts of $\sim$200 Å. Hence, the areal density of latent tracks, revealed in Fig. 3, appears to be close to the density of ion impacts. Throughout the bombarded epilayer, high-resolution XTEM has also revealed planar defects which are parallel to the basal plane of the GaN film [15].

It has also been demonstrated in [15] that the gross level of lattice disorder in GaN bombarded with 200 MeV Au ions, as measured by RBS/C, gradually increases with increasing ion fluence up to $\sim 10^{13}$ cm^{-2}. This damage buildup has been best described by the direct impact (zero overlap) model. For ion fluences above 10^{13} cm^{-2}, delamination of the GaN epilayer has been observed and attributed to ion-beam-induced rearrangement and weakening of atomic bonds at the film/substrate interface and the buildup of mechanical stress in both sapphire substrate and GaN film.

5. Blistering of H-implanted GaN

A knowledge of the influence of implant and annealing conditions on the blistering of H-implanted GaN is essential for the development of ion slicing and "etching" of GaN using implantation with H ions. In particular, ion slicing [16] is a rather attractive technological tool for the integration of GaN-based electronics (with GaN epilayers being usually grown on sapphire or SiC substrates) with Si-based integrated circuit technology.

The mechanisms of blistering of wurtzite GaN films implanted with H ions have been studied in Ref. [17]. In particular, the influence of the following parameters on the blistering process has been investigated: (i) ion energy (from 20 to 150 keV), (ii) ion dose (up to 1.2×10^{18} cm^{-2}), (iii) implantation temperature (from -196°C to 250°C), and (iv) annealing temperature (up to 900°C). Results from Ref. [17] have shown that the blistering behaviour strongly depends on both implant and annealing conditions, such as ion energy, ion dose, and implantation and annealing temperatures.

For example, the effect of ion dose on the blistering process is illustrated in Figs. 4(a) and (b) for the case of 100 keV H ion implantation at RT. With increasing dose of 100 keV H ions at RT, surface blisters become elongated in shape. At a very large dose of 1.2×10^{18} cm^{-2} [Fig. 4(b)], blisters appear to grow and overlap to produce large exfoliated areas. Hence, Fig. 4 clearly illustrates that the pattern of surface blistering of GaN strongly depends on ion dose.

Fig. 4 also illustrates that implantation temperature has a very strong effect on the blistering process in GaN during post-implantation annealing. Indeed, annealing at $\gtrsim$900°C is required for blistering of GaN bombarded with 100 keV H ions at LN_2 to a dose of 5×10^{17} cm^{-2}, while, after identical implantation at RT, surface blistering occurs at much lower annealing temperatures

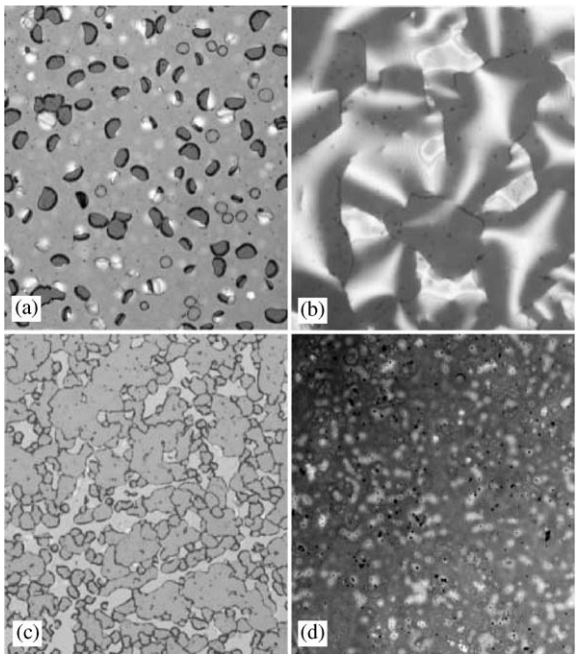

Fig. 4. Typical optical micrographs of GaN samples implanted at 20°C [(a), (b)] and at -196°C [(c), (d)] with 100 keV H ions to doses of 8×10^{17} [(a), (d)], 1.2×10^{18} (b), and 5×10^{17} cm^{-2} (c). After implantation, samples were annealed at 900°C for 5 min in a nitrogen ambient. The horizontal field width is 250 μm for (a), (c), and (d) and is 500 μm for (b).

($\gtrsim$350°C). Moreover, the data in Fig. 4 reveals that surface blistering patterns are markedly different for RT and LN_2 bombardment regimes. Hence, an increase in implantation temperature not only enhances blistering but also changes the pattern of surface exfoliation during post-implantation annealing.

6. Electrical isolation of GaN and ZnO

Ion irradiation can render the material highly resistive under appropriate conditions and, hence, can be used for selective-area electrical isolation [18]. Electrical isolation of n-type GaN and ZnO by MeV light-ion irradiation has recently been reported in Refs. [19–22] and [23,24], respectively. It has been demonstrated that sheet resistance of both GaN and ZnO can be increased by > 7 orders of magnitude as a result of ion irradiation [19,23]. Results have also shown that, for both GaN and ZnO, the ion doses necessary for electrical isolation inversely depend on the number of lattice displacements produced by the ion beam. As an example, Fig. 5 shows sheet resistances of GaN and ZnO epilayers as a function of displacements per atom (DPA) for irradiation with MeV Li, C, O, and Si ions. Fig. 5 clearly illustrates that the isolation process in both GaN and ZnO is essentially independent of ion mass (within experimental error), provided that ion doses are converted to DPA. It is also seen from Fig. 5 that the efficiency of the formation of lattice defects, responsible for electrical isolation, is rather different in GaN and ZnO, with ZnO being significantly more resistant to defect-induced electrical isolation. Indeed, Fig. 5 shows that two orders of magnitude more atomic displacements are needed to isolate ZnO as compared to the case of GaN with a similar original free electron concentration.

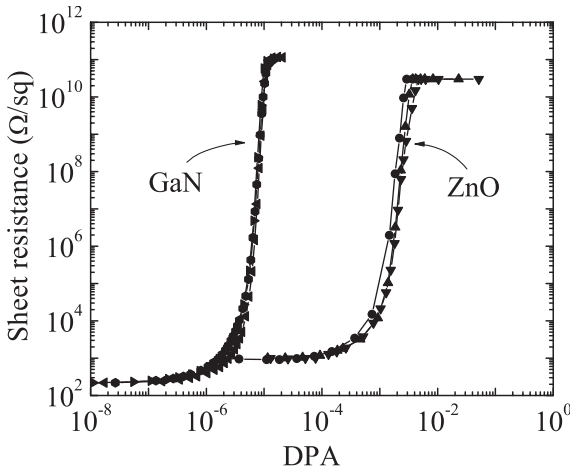

Fig. 5. Sheet resistance of GaN and ZnO epilayers (with original free carrier concentrations of $\sim$3 and $\sim 1 \times 10^{17}$ cm^{-3}, respectively) as a function of displacements per atom (DPA). Samples were bombarded at room temperature with MeV Li, C, O, and Si ions. See [19,23] for the details of implant conditions. When plotted as a function of DPA, isolation curves for these ions essentially overlap (within experimental error).

The effects of irradiation temperature, beam flux, and collision cascade density on electrical isolation of GaN by MeV light-ion irradiation have been reported in Ref. [20]. These results [20] have revealed that both implantation temperature (varied from −196°C up to 150°C) and ion beam flux affect the process of electrical isolation in the case of irradiation with ^{12}C ions. This effect has suggested that the centres responsible for electrical isolation are defect *complexes* or anti-site-related defects, whereas ion-beam-generated simple Frenkel pairs in GaN are mobile and unstable during irradiation at LN_2 and above. The influence of irradiation temperature and beam flux revealed in Ref. [20] should be taken into account for choosing implant conditions necessary for an effective electrical isolation of GaN-based devices.

An unusual approach to study electrical isolation in GaN by energy dispersive X-ray spectrometry (EDS) has been developed in Ref. [21]. This study has shown that the maximum bremsstrahlung X-ray energy (the Duane–Hunt limit) can be used to monitor the isolation process in the scanning electron microscope. A correlation of EDS and resistance measurements of GaN [21] has strongly suggested that the magnitude of sample charging scales with the number of ion-beam-produced deep electron traps which are empty at equilibrium. This method allows the dose region above the threshold dose for isolation to be conveniently studied, whereas the application of conventional (low-voltage) electrical techniques in this dose range with large sheet resistances of the

material ($\gtrsim 10^{11}$ Ω/sq) is often impossible due to comparable parasitic resistances of the experimental setup. In addition, such contactless EDS measurements allow the whole semiconductor wafer to be studied without cutting and give an ideal opportunity to study electrical isolation in some cases when the fabrication of Ohmic contacts is not feasible [21].

A quantitative model for electrical isolation of GaN by light-ion bombardment has been developed in Ref. [22]. In this model, a decrease in the concentration of free carriers responsible for isolation has been assumed to be due to the formation of complexes of ion-beam-generated point defects with shallow donor or acceptor dopants. The defect interaction processes have been described in terms of quasi-chemical reactions. Results have shown that the model developed in Ref. [22] can adequately describe experimental data for electrical isolation in the case of MeV light-ion irradiation of *n*-GaN. In particular, this model [22] describes well the dependence of sheet resistance on ion dose and the number of ion-beam-generated atomic displacements as well as the dependence of the threshold isolation dose on original free electron concentration and on the number of atomic displacements. Future studies should be able to extend the theoretical approach developed in Ref. [22] to include ion beam flux and temperature dependences as well as to potentially describe electrical isolation in other semiconductors.

The thermal stability of ion-irradiation-induced electrical isolation of n-type single-crystal ZnO epilayers has been studied in Ref. [24]. Results have shown that an increase in the dose of 2 MeV ^{16}O ions (up to ~2 orders of magnitude above the threshold isolation dose) and irradiation temperature (up to 350°C) has a relatively minor effect on the thermal stability of electrical isolation, which is limited to temperatures of ~300–400°C. An analysis of the temperature dependence of sheet resistance has suggested that effective levels associated with irradiation-produced defects are rather shallow (<50 meV). Results from Ref. [24] have also revealed a negligible ion-beam flux effect in the case of irradiation with 2 MeV ^{16}O ions, supporting high diffusivity of ion-beam-generated defects during ion irradiation and a very fast stabilization of collision cascade processes in ZnO. For the case of implantation with keV Cr, Fe, or Ni ions, the evolution of sheet resistance with annealing temperature is consistent with defect-induced isolation, with a relatively minor effect of Cr, Fe, or Ni impurities on the thermal stability of isolation. At this stage, more work is highly desirable to study the effect of other impurities which can potentially form thermally-stable deep acceptor levels in ZnO if desirable device processing and/or operating temperatures are above ~400°C.

7. Effect of Al and In content on dynamic annealing in III-nitrides

Recently, ion-bombardment-produced defects have also been studied in InGaN, AlGaN, and AlN [25–31]. As an example of the defect microstructure produced in III-nitrides [31], Fig. 6 shows that bombardment of $Al_{0.19}Ga_{0.81}N$ at RT with 300 keV Au ions to a dose of 1.5×10^{16} cm^{-2} results in the formation of a buried amorphous layer [compare bright- and dark-field images in Figs. 6(a) and (b)]. Fig. 6 also illustrates the formation of planar defects which are parallel to the basal plane of the $Al_{0.19}Ga_{0.81}N$ film. Similar planar defects have also been observed in GaN bombarded under a wide range of irradiation conditions (see Section 3) as well as in $Al_xGa_{1-x}N$ (with $x = 0.08$ and 0.19) and $In_{0.16}Ga_{0.84}N$ bombarded at RT with 300 keV Au ions to relatively low doses [28,29].

Fig. 6 also clearly illustrates a number of circular inclusions within the buried amorphous layer. The formation of similar circular inclusions has also been observed by XTEM in GaN amorphized by ion bombardment [4]. This effect has been attributed to ion-beam-induced stoichiometric imbalance with the formation of N_2 gas bubbles stimulated by the high plasticity of an amorphous phase of GaN [4]. Note that, for the sample from Fig. 6, surface exfoliation as a result of bubble growth, typically observed for GaN bombarded to high ion doses, is hindered by a stiff surface layer of a crystalline material. Fig. 6

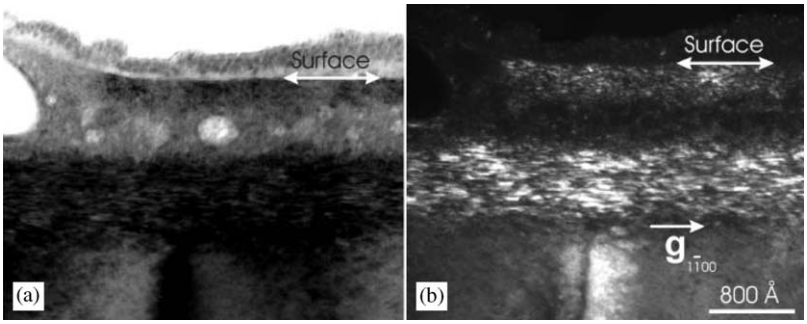

Fig. 6. Bright-field (a) and dark-field (b) XTEM images ($\mathbf{g} = 1\bar{1}00^*$) of $Al_{0.19}Ga_{0.81}N$ bombarded at RT with 300 keV Au ions with a beam flux of $\sim 3.1 \times 10^{12}$ cm^{-2} s^{-1} to a dose of 1.5×10^{16} cm^{-2}. Both images are of the same magnification and illustrate the same sample region. Note increased surface roughness of this sample due to the formation of circular inclusions within the buried amorphous layer.

illustrates that, similar to the case of GaN, N_2 bubble formation occurs at RT in amorphous $Al_{0.19}Ga_{0.81}N$.

The damage buildup behaviour in AlGaN is illustrated in Fig. 7, which summarizes defect accumulation curves at RT (Fig. 7(a)) and LN_2 (Fig. 7(b)) for samples with different Al content. Shown in Fig. 7 are dependences of relative disorder, extracted from RBS/C data, in the bulk defect peak region ($\sim$450 Å from the sample surface) as a function of DPA. These DPA values are $N_{Ga}^{vac}\Phi/n_{Ga}^{at}$, where N_{Ga}^{vac} is the average concentration of Ga vacancies generated by one ion per unit of depth in the bulk defect peak region, n_{Ga}^{at} is the concentration of Ga atoms in the AlGaN alloy, and Φ is ion dose. Such a conversion of ion doses into DPA takes account of the difference in the number of atomic displacements ballistically generated by the ion beam in different AlGaN alloys. This allows the influence of factors other than the expected difference in ballistic processes to be studied. For DPA $\lesssim 0.3$, when the lateral overlap of collision cascades is small, DPA values essentially indicate how many times each lattice atom has been ballistically displaced by the ion beam. For larger DPA values, however, in the absence of dynamic annealing (when all ion-beam-generated defects are essentially ''frozen'' in the lattice), the relative number of displaced atoms in the lattice accumulates as $1 - \exp(-\mathrm{DPA})$ due to an effective lateral overlap of collision cascades produced by different ions.

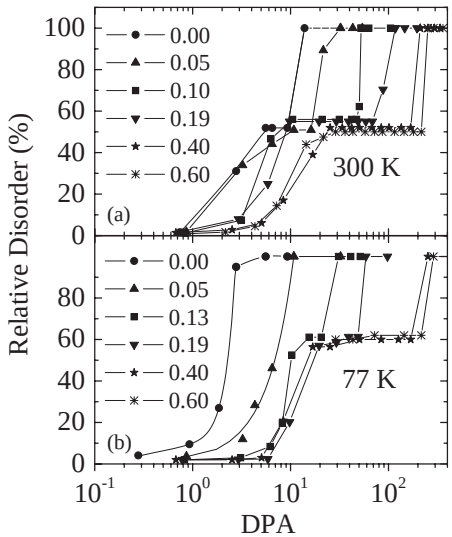

Fig. 7. Relative disorder (extracted from RBS/C spectra for the Ga peak) in the bulk defect peak region for $Al_xGa_{1-x}N$ samples as a function of displacements per atom (DPA). Samples were bombarded with 300 keV Au ions at RT (a) and LN_2 (b) with a beam flux of $\sim 3.1 \times 10^{12}$ cm^{-2} s^{-1}. Aluminium content (x) in different samples is given in the legend.

Fig. 7(a) illustrates that, for all values of x at RT, defect saturation occurs at a relative disorder level of $\sim$50–60%, and damage–DPA curves gradually shift toward larger DPA values with increasing x. For the case of bombardment at LN_2, Fig. 7(b) clearly illustrates a transition from the regime of a gradual damage build-up up to amorphization for $x \lesssim 0.1$ to the regime with

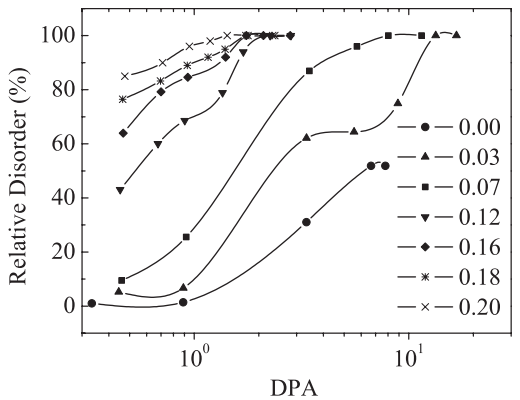

Fig. 8. Relative disorder (extracted from RBS/C spectra for the Ga peak) in the bulk defect peak region for $In_xGa_{1-x}N$ samples as a function of displacements per atom (DPA). Samples were bombarded with 300 keV Au ions at RT with a beam flux of $\sim 3.1 \times 10^{12}$ cm^{-2} s^{-1}. Indium content (x) in different samples is given in the legend. Lines are shown to guide the reader's eye.

saturation of damage in the bulk (at a disorder level of $\sim 60\%$) for $x \gtrsim 0.1$. The fact that the disorder level in the saturation regime is essentially independent of Al content and sample temperature (see Fig. 7) suggests that similar defect structures are present in $Al_xGa_{1-x}N$ in the saturation regime, when defect generation and dynamic annealing processes are effectively balanced.

Fig. 8 shows damage build-up curves in InGaN films with different In concentrations as a function of DPA. Similar to the case of AlGaN discussed above, such a conversion of ion doses to DPA takes into account the difference in ballistic processes in different InGaN alloys. It is seen from Fig. 8 that an increase in In content suppresses dynamic annealing processes and weakens the effect of damage saturation (at the depth of the bulk disorder peak).

Results from Figs. 7 and 8 show that adding Al increases (while adding In decreases) the level of dynamic annealing in AlGaN (and InGaN) ternary alloys. This result has been attributed to a larger (smaller) energy of the Al–N (In–N) bond as compared to the energy of the Ga–N bond [31]. Indeed, the buildup of preamorphous disorder in III-nitrides is associated with the formation of lattice defects involving broken and reconstructed bonds. It is expected that dynamic annealing processes, including defect annihilation, will be more efficient in a system with a larger energy gain due to the recovery of broken, distorted, and non-stoichiometric bonds, which are ballistically generated by the ion beam.

This argument, based on the energies of chemical bonds, has also been applied in [31] to explain dynamic annealing in $Al_xGa_{1-x}As$ alloys, studied in detail previously (see, for example, [32]). It should be noted, however, that, although the efficiency of dynamic annealing in AlGaN, InGaN, and AlGaAs alloys scales with the energy of chemical bonds, variations in other parameters can also be responsible for changes in the damage buildup behaviour. For example, activation energies for various defect migration and interaction processes (which are not well known in AlGaN and InGaN) can also dramatically affect damage accumulation. Hence, although the bond energy gives a clear trend in the efficiency of dynamic annealing and the buildup of pre-amorphous disorder in a number of semiconductor systems such as AlGaN, InGaN, and AlGaAs, a better understanding of the physical mechanisms controlling dynamic annealing in these semiconductors will need to await more detailed data on defect migration and interaction processes.

8. Damage buildup in ZnO

A detailed study of the evolution of lattice defects in single-crystal ZnO bombarded with 60 keV ^{28}Si and 300 keV ^{197}Au ions at LN_2 and RT has been reported in Ref. [33]. It has been shown in Ref. [33] there that ZnO exhibits strong dynamic annealing, and even high-dose bombardment with heavy (^{197}Au) ions at LN_2 does not render ZnO amorphous. However, a crystalline-to-amorphous phase transition can be induced by irradiation with relatively light ^{28}Si ions. In this latter case, amorphization has been attributed to strong chemical effects of Si atoms implanted into the ZnO lattice, resulting in the stabilization of an amorphous phase. High-dose heavy-ion bombardment also results in strong stoichiometric imbalance (loss of O) in the near-surface region. A variation in irradiation temperature from LN_2 up

to RT has been shown to have a minor effect on the damage build-up behaviour in ZnO bombarded with Au ions. Data analysis in Ref. [33] has also shown that a variation in the density of collision cascades by increasing ion mass from ^{28}Si up to ^{197}Au has a negligible effect on the damage buildup behaviour, in contrast to the case of GaN, discussed in Section 2. For both light (^{28}Si) and heavy (^{197}Au) ion bombardment regimes, XTEM has revealed that ion irradiation produces energetically favourable planar defects which are parallel to the basal plane of the wurtzite structure of ZnO. More details of the damage build-up behaviour in ZnO can be found in [33].

9. Anomalous defect peak in ZnO

Interestingly, our RBS/C study reported in Ref. [33] has also revealed the formation of an intermediate defect peak (IDP) between the surface and bulk peaks of disorder in Au-implanted ZnO. As an example, Fig. 9 illustrates this effect. It is also seen from Fig. 9 that the position of the IDP changes with increasing ion dose. Indeed, as ion bombardment proceeds, the IDP originates at the sample surface and moves toward the bulk defect peak. For relatively large ion doses (0.5–1×10^{16} cm^{-2}), Fig. 9 shows that the position of the IDP appears to be independent of ion dose and equals to $\sim$380 Å. In addition, for the sample temperatures studied in Ref. [33] (LN_2 and RT), the behaviour of the IDP is independent of irradiation temperature, within experimental error.

The formation of this middle peak is rather unexpected and, to our knowledge, has not been observed in any other material. Indeed, typical depth profiles of ion-beam-produced lattice disorder in crystalline solids have a close-to-Gaussian shape with one maximum (in addition to the surface defect peak), reflecting the depth profile of atomic displacements ballistically generated by the ion beam.

Results from Ref. [33] have essentially ruled out the possibilities that the IDP in RBS/C spectra is related to measurement artifacts, such as segregation of Au, large surface non-uniformities, or

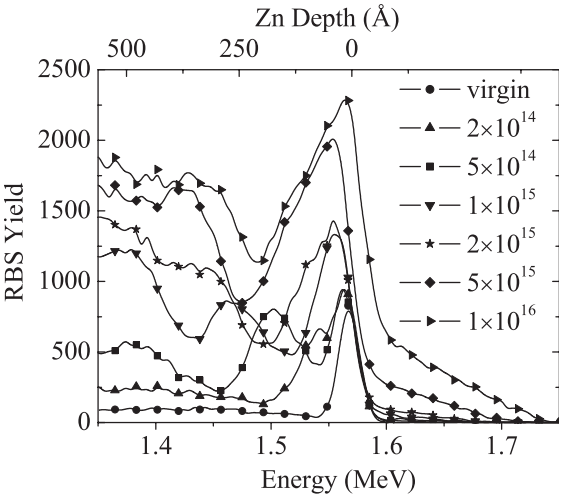

Fig. 9. Selected RBS/C spectra acquired with an 8° glancing angle detector geometries showing the damage buildup in the near-surface layer of ZnO bombarded at LN_2 with 300 keV Au ions with a beam flux of $\sim 3 \times 10^{12}$ cm^{-2} s^{-1}. Implantation doses (in cm^{-2}) are indicated in the legend. Note that the near-surface random yield corresponds to $\sim$2800 counts.

pronounced ion-beam-induced stoichiometric changes. This suggests that the mechanism for IDP formation is disorder-related. It has been suggested that the IDP can be caused by the formation of a localized band of lattice defects resulting from imperfect defect annihilation processes during ion bombardment [33]. A possible nucleation site for such a defect cluster formation, giving rise to a direct scattering peak in RBS/C spectra, can be an excess of ion-beam-generated lattice vacancies near the sample surface. Indeed, it is well known that vacancies and interstitials are spatially separated in a collision cascade, with an interstitial excess at the ion end of range and a vacancy excess closer to the surface. This effect is expected to be pronounced for bombardment regimes with strong dynamic annealing, which is the case for ZnO at least at LN_2 and above. The importance of such a ballistic separation of interstitials and vacancies in the damage build-up behaviour in ZnO bombarded with ^{197}Au ions is also supported by the fact that the bulk defect peak is shifted, relative to the maximum of the nuclear energy loss profile, closer to the ion end of range, the region with an interstitial excess.

This scenario for a defect-related formation of the IDP appears to be consistent with the experimental observations from Ref. [33]. The fact that the IDP is observed only in ZnO samples bombarded with (heavy) ^{197}Au ions (not in samples irradiated with lighter ^{28}Si ions) [33] may suggest that the nucleation of the defect band giving rise to the IDP requires a large vacancy excess and the formation of dense collision cascades generated by heavy ions. The fact that the IDP moves deeper into the crystal bulk, with increasing ion dose, can be associated with the onset of ion-beam-induced loss of O from the sample surface as ion irradiation proceeds. Loss of O can stimulate defect annihilation processes in the region between the sample surface and the defect band giving rise to a separation of the IDP from the surface peak. Indeed, such O-loss has been measured by X-ray photoelectron spectroscopy for higher ion doses when ion-beam-induced stoichiometric changes become significant [33]. However, this intriguing dose dependence of the IDP position can also be attributed to a possible increased defect annihilation at the sample surface. Additional work is presently needed to clarify the role of the sample surface and material stoichiometry in the formation and evolution of the IDP.

10. Comparison of GaN with ZnO

A rather detailed comparison of the damage build-up behaviour in GaN with that in other semiconductors as well as metals has previously been given in Ref. [4]. In the present review, it is instructive to make a brief comparison of ion-beam-induced defect processes in GaN and ZnO. Both ZnO and GaN exhibit strong dynamic annealing. This behaviour is typical for materials with a large degree of ionicity [31]. However, ZnO is even more resistive to ion-beam-induced damaging than GaN. Moreover, ZnO does not exhibit the effect of defect saturation in the crystal bulk which has been observed in GaN. The surface of ZnO is also not a nucleation site for amorphization, as it is in GaN. Indeed, for a wide range of ion bombardment conditions, with increasing ion dose, amorphization of GaN proceeds layer-by-layer from the sample surface into the crystal bulk [6]. In the case of ZnO, amorphization nucleates at the ion end of range, mediated by chemical effects of implanted Si atoms [33]. Furthermore, in contrast to the case of GaN, a negligible effect of the density of collision cascades on the damage build-up behaviour in ZnO has been revealed in [33]. However, both these materials exhibit ion-beam-induced stoichiometric imbalance as a result of high-dose heavy-ion bombardment, and, in both cases, implanted species can dramatically change the behaviour of damage accumulation and stabilize an amorphous phase. Moreover, in both GaN and ZnO, defect structures resultant from imperfect dynamic annealing processes include planar defects parallel to the basal plane of the wurtzite lattice structure.

11. Conclusions

This brief review has focused on our recent studies of ion-beam-produced defects of group-III nitrides and ZnO. Due to efficient dynamic annealing, these wurtzite semiconductors exhibit a range of intriguing and complex defect-related processes. Although our understanding of ion-beam damaging behaviour in III-nitrides and ZnO has matured considerably in the past several years, much more work is obviously needed before ion-damage effects in these materials are fully understood.

Acknowledgements

We are grateful to a number of people involved in this work through collaboration and discussion, including J. Zou, G. Li, H. Boudinov, A. I. Titov, H. Timmers, M. Toth, M. R. Phillips, Y. G. Wang, P. N. K. Deenapanray, S. J. Pearton, C. Evans, A. J. Nelson, and A. V. Hamza. Work at LLNL was performed under the auspices of the U.S. Department of Energy by the University of California, Lawrence Livermore National Laboratory under Contract No. W-7405-Eng-48.

References

[1] Pearton SJ, Zolper JC, Shul RJ, Ren F. J Appl Phys 1999;86:1.
[2] Jain SC, Willander M, Narayan J, Van Overstraeten R. J Appl Phys 2000;87:965.
[3] Rauschenbach B. In: Manasreh MO, editor. III-nitride semiconductors: electrical, structural and defects properties. Amsterdam: Elsevier; 2000.
[4] Kucheyev SO, Williams JS, Pearton S. Mater Sci Eng R 2001;33:51.
[5] Ronning C, Carlson EP, Davis RF. Phys Rep 2001; 351:349.
[6] Kucheyev SO, Williams JS, Jagadish C, Zou J, Li G, Titov AI. Phys Rev B 2001;64:035202.
[7] Kucheyev SO, Williams JS, Titov AI, Li G, Jagadish C. Appl Phys Lett 2001;78:2694.
[8] Kucheyev SO, Williams JS, Zou J, Li G, Jagadish C, Titov AI. Nucl Instrum Methods Phys Res B 2002;190:782.
[9] Biersack JP, Haggmark LG. Nucl Instrum Methods 1980;174:257.
[10] Kucheyev SO, Williams JS, Jagadish C, Zou J, Li G. Phys Rev B 2000;62:7510.
[11] Wang CM, Jiang W, Weber WJ, Thomas LE. J Mater Res 2002;17:2945.
[12] Wang YG, Zou J, Kucheyev SO, Williams JS, Jagadish C, Li G. Electrochem Solid-State Lett 2003;6:G34.
[13] Fleischer RL, Price PB, Walker RM. Nuclear Tracks in Solids. Berkeley: University of California Press; 1975.
[14] Fischer BE, Spohr R. Rev Mod Phys 1983;55:907.
[15] Kucheyev SO, Timmers H, Zou J, Williams JS, Jagadish C, Li G, unpublished.
[16] Bruel M. Nucl Instrum Methods B 1996;108:313.
[17] Kucheyev SO, Williams JS, Jagadish C, Zou J, Li G. J Appl Phys 2002;91:3928.
[18] Pearton SJ. Mater Sci Rep 1990;4:313.
[19] Boudinov H, Kucheyev SO, Williams JS, Jagadish C, Li G. Appl Phys Lett 2001;78:943.
[20] Kucheyev SO, Boudinov H, Williams JS, Jagadish C, Li G. J Appl Phys 2002;91:4117.
[21] Kucheyev SO, Toth M, Phillips MR, Williams JS, Jagadish C, Li G. J Appl Phys 2002;91:3940.
[22] Titov AI, Kucheyev SO. J Appl Phys 2002;92:5740.
[23] Kucheyev SO, Deenapanray PNK, Jagadish C, Williams JS, Yano M, Koike K, Sasa S, Inoue M, Ogata K. Appl Phys Lett 2002;81:3350.
[24] Kucheyev SO, Deenapanray PNK, Jagadish C, Williams JS, Yano M, Koike K, Sasa S, Inoue M, Ogata K. J Appl Phys 2003;93:2972.
[25] Zolper JC, Pearton SJ, Abernathy CR, Vartuli CB. Appl Phys Lett 1995;66:3042.
[26] Vartuli CB, Pearton SJ, Abernathy CR, MacKenzie JD, Zolper JC. J Vac Sci Technol B 1995;13:2293.
[27] Polyakov AY, Shin M, Skowronski M, Wilson RG, Greve DW, Pearton SJ. Solid-State Electronics 1997; 41:703.
[28] Kucheyev SO, Williams JS, Zou J, Pearton SJ, Nakagawa Y. Appl Phys Lett 2001;79:602.
[29] Kucheyev SO, Williams JS, Zou J, Li G, Jagadish C, Manasreh MO, Pophristic M, Guo S, Ferguson IT. Appl Phys Lett 2002;80:787.
[30] Kucheyev SO, Williams JS, Zou J, Jagadish C, Pophristic M, Guo S, Ferguson IT, Manasreh MO. J Appl Phys 2002;92:3554.
[31] Kucheyev SO, Williams JS, Zou J, Jagadish C. J Appl Phys; accepted for publication.
[32] Tan HH, Jagadish C, Williams JS, Zou J, Cockayne DJH, Sikorski A. J Appl Phys 1995;77:87.
[33] Kucheyev SO, Williams JS, Jagadish C, Zou J, Evans C, Nelson AJ, Hamza AV. Phys Rev B 2003;67:094115.